

AD-A108080

TECHNICAL
LIBRARY

AD A-108080

TECHNICAL REPORT ARBRL-TR-02375

STREAMWISE VORTICITY DECAY DOWNSTREAM OF A
THREE-DIMENSIONAL PROTUBERANCE

C. W. Kitchens, Jr.
N. Gerber
R. Sedney
J. M. Bartos

October 1981



US ARMY ARMAMENT RESEARCH AND DEVELOPMENT COMMAND
BALLISTIC RESEARCH LABORATORY
ABERDEEN PROVING GROUND, MARYLAND

Approved for public release; distribution unlimited.

Destroy this report when it is no longer needed.
Do not return it to the originator.

Secondary distribution of this report by originating
or sponsoring activity is prohibited.

Additional copies of this report may be obtained
from the National Technical Information Service,
U.S. Department of Commerce, Springfield, Virginia
22151.

The findings in this report are not to be construed as
an official Department of the Army position, unless
so designated by other authorized documents.

*The use of trade names or manufacturers' names in this report
does not constitute endorsement of any commercial product.*

UNCLASSIFIED

SECURITY CLASSIFICATION OF THIS PAGE (When Date Entered)

REPORT DOCUMENTATION PAGE		READ INSTRUCTIONS BEFORE COMPLETING FORM
1. REPORT NUMBER TECHNICAL REPORT ARBRL-TR-02375	2. GOVT ACCESSION NO.	3. RECIPIENT'S CATALOG NUMBER
4. TITLE (and Subtitle) STREAMWISE VORTICITY DECAY DOWNSTREAM OF A THREE-DIMENSIONAL PROTUBERANCE		5. TYPE OF REPORT & PERIOD COVERED Final
		6. PERFORMING ORG. REPORT NUMBER
7. AUTHOR(s) C.W. Kitchens, Jr., N. Gerber, R. Sedney, and J.M. Bartos		8. CONTRACT OR GRANT NUMBER(s)
9. PERFORMING ORGANIZATION NAME AND ADDRESS U.S. Army Ballistic Research Laboratory (ATTN: DRDAR-BLL) Aberdeen Proving Ground, Maryland 21005		10. PROGRAM ELEMENT, PROJECT, TASK AREA & WORK UNIT NUMBERS RDT&E 1L161102AH43
11. CONTROLLING OFFICE NAME AND ADDRESS US Army Armament Research & Development Command US Army Ballistic Research Laboratory (DRDAR-BL) Aberdeen Proving Ground, MD 21005		12. REPORT DATE October 1981
		13. NUMBER OF PAGES 46
14. MONITORING AGENCY NAME & ADDRESS (If different from Controlling Office)		15. SECURITY CLASS. (of this report) Unclassified
		15a. DECLASSIFICATION/DOWNGRADING SCHEDULE
16. DISTRIBUTION STATEMENT (of this Report) Approved for public release; distribution unlimited.		
17. DISTRIBUTION STATEMENT (of the abstract entered in Block 20, if different from Report)		
18. SUPPLEMENTARY NOTES		
19. KEY WORDS (Continue on reverse side if necessary and identify by block number) Streamwise Vorticity Three-Dimensional Protuberance Boundary-Layer Boundary-Region Calculation		
20. ABSTRACT (Continue on reverse side if necessary and identify by block number) Streamwise vortices generated in boundary layers are known to persist for hundreds of boundary-layer thicknesses. This remarkable property is the main topic of this report. The particular case of the flow field generated by a three-dimensional protuberance immersed in a flat plate boundary layer is studied using numerical modeling. Experimental measurements in a downstream crossflow plane are used to construct initial data for a marching calculation using the boundary-layer and boundary-region approximations; the latter includes crossflow diffusion terms. The former fails to predict the flow		

UNCLASSIFIED

SECURITY CLASSIFICATION OF THIS PAGE(When Data Entered)

20. ABSTRACT (Continued)

field, but results from the latter agree qualitatively in aspects of the flow field determined from the measurements of Tani, et al., and are also in fair quantitative agreement.

UNCLASSIFIED

SECURITY CLASSIFICATION OF THIS PAGE(When Data Entered)

TABLE OF CONTENTS

	<u>Page</u>
LIST OF ILLUSTRATIONS.....	5
I INTRODUCTION.....	7
II GOVERNING EQUATIONS.....	8
III TANI TEST PROBLEM.....	10
IV INITIAL PLANE OF DATA.....	11
V NUMERICAL PROCEDURE AND BOUNDARY CONDITIONS.....	14
VI RESULTS AND COMPARISON WITH EXPERIMENT.....	16
VII CONCLUSIONS.....	18
REFERENCES.....	20
LIST OF SYMBOLS.....	31
APPENDIX A.....	33
APPENDIX B.....	35
APPENDIX C.....	37
DISTRIBUTION LIST.....	41

LIST OF ILLUSTRATIONS

<u>Figure</u>		<u>Page</u>
1	Sketch of Protuberance in Boundary Layer in Tani Experiment ($k/\delta = 0.39$, $Re_{x_k} = 2.08 \times 10^5$, $Re_k = 550$)	21
2	Measured Spanwise Distribution at $x_I = x_k + 10k$ of (a) Streamwise Velocity Component and (b) Flow Inclination in the x,y Plane at Two Heights; (c) Experimental Dis- tribution Across Boundary Layer of Peak-Valley Velocity Difference ($U_1 - U_2$).....	22
3	Analytical Spanwise Distributions of (a) u/u_∞ and (b) $\beta \equiv \tan^{-1}(V/U)$, Eqs (17) and (18), at Fixed Heights- in the Initial Data Plane, and Comparison with Tani Data.....	23
4	Analytical Distribution of (a) u/u_∞ and (b) $U_1 - U_2$ Through the Boundary Layer in the Initial Data Plane, and Comparison with Tani Data.....	24
5	Crossflow Plane (y,z) Velocity Vector Projections in Initial Data Plane at $x = x_k + 10k$	25
6	Spanwise Distribution of Second-Derivatives of Streamwise Velocity Component in Initial Data Plane.....	26
7	Crossflow Plane (y,z) Velocity Vector Projections at $x = x_k + 16k$	27
8	Streamwise Variation of Maximum Vorticity at Wall.....	28
9	Streamwise Variation of Horseshoe Vortex Spacing.....	28
10	Streamwise Variation of Maximum Peak-Valley Velocity Difference Induced by Horseshoe Vortex.....	29
11	Comparison of Horseshoe Vortex Spacing: 3-D Boundary Layer (Scheme D) vs Boundary Region.....	29

I. INTRODUCTION

A protuberance in a boundary layer whose height is of the order of the boundary layer thickness would be expected to cause large changes in the neighboring flow field. Experimentally it has been found that significant perturbations in the flow are also induced downstream of the protuberance for hundreds of protuberance heights. As determined by flow visualization and supported by hot wire measurements, these perturbations take the form of streamwise vortices or concentrations of streamwise vorticity. A theoretical model for this persistent effect does not exist; in this report numerical modelling is employed.

There are other flow fields where the persistence of streamwise vorticity has been found. In wind tunnel experiments on flat plates, non-uniformities in screens far upstream of the plate have caused significant spanwise velocity components. Small non-uniformities on the leading edge of plates or on steps of bodies of revolution also induce persistent streamwise vortices. Such vortices are also formed in the boundary layer on the leeward side of a body of revolution at moderate angle of attack and can persist to the base; as angle of attack increases, the vortices are shed from the body. These vortices can influence the Magnus effect on a projectile.

The persistence of streamwise vortices is found for both laminar and turbulent boundary layers. For the latter, spanwise non-uniformity in the transition process can induce them in addition to the mechanisms mentioned above. Streamwise vorticity may also be involved in large-scale structures in turbulent boundary layers. A matter of practical concern when streamwise vortices exist in turbulent boundary layers is that they increase the heat transfer.

The above ideas are discussed by Morkovin¹, who also emphasizes the unsatisfactory state of the observations and theory for streamwise vortices. The main conclusions of the present work are also discussed.

To study the effect, the simplest situation is chosen in which streamwise vortices are found: flow behind a protuberance imbedded in a low speed laminar boundary layer on a flat plate. Also, more experimental data is available for this case than any other; even so it is not sufficient for our purposes. The objective of this work is to determine if numerical simulation of the flow field will show the persistence and other features of the flow field that are observed experimentally.

A schematic of the flow field is shown in Figure 1. Qualitatively, the same flow field features are found over a wide range of conditions, regardless of whether the boundary layer is laminar or turbulent, or whether the external

1. Morkovin, M.V., "Observations on Streamwise Vortices in Laminar and Turbulent Boundary Layers", NASA Contractor Report 159061, April 1979.

flow is high speed or low speed. Sedney² has surveyed the effects of small protuberances on boundary layer flows; for additional details of the flow field and references describing them see Reference 2. As sketched in Figure 1, the boundary layer separates upstream of the protuberance, forming a horse-shoe vortex which stretches around the obstacle. Spiral vortices rise up from the surface of the plate in the near wake, forming twin-vortex filaments which trail downstream. Smoke visualization studies in low-speed boundary layers show that the streamwise vortices produced by the interaction process can remain steady and distinct for hundreds of protuberance heights downstream of the obstacle. The persistence of these vortices is quite remarkable, even more so when it occurs in turbulent boundary layers, considering the high diffusivity.

Two numerical approaches for modeling the downstream flow field are employed in the present study. The first uses 3-D boundary-layer approximations; the second makes use of a 3-D boundary-region approximation which includes the viscous crossflow (diffusion) terms neglected in the boundary-layer theory. The measurements of Tani, et al.³, taken ten protuberance heights downstream of the obstacle, are used to construct the initial data for the calculations. Quantitative agreement between the numerical simulation and measurements will depend on the accuracy with which we can fit the initial data, which is obtained from experimental measurements and properties of boundary layers. The uncertainties in the fitting will be described.

The major conclusion is that, using the boundary-region approximation, we are able to reproduce the qualitative features of the flow field far downstream of the obstacle, including the persistence of streamwise vorticity; but we do not succeed using the 3-D boundary-layer approximation.

II. GOVERNING EQUATIONS

For some range of the parameters involved, such as Reynolds number, protuberance dimensions and geometry, the flow is sensibly steady; see Reference 2. Therefore we use the steady, 3-D, incompressible Navier-Stokes equations.*

$$u u_x + v u_y + w u_z = -\rho^{-1} p_x - \mu(u_{xx} + u_{yy} + u_{zz}), \quad (1)$$

2. Sedney, R., "A Survey of the Effects of Small Protuberances on Boundary-Layer Flows", *AIAA Journal*, Vol. 11, No. 6, June 1973, pp. 782-792.

3. Tani, I., Komoda, H., and Komatsu, Y., "Boundary-Layer Transition by Isolated Roughness", *Aeronautical Research Institute Report No. 375*, University of Tokyo, November 1962.

*Definitions of symbols are given in the LIST OF SYMBOLS section.

$$u v_x + v v_y + w v_z = -\rho^{-1} p_y + \mu(v_{xx} + v_{yy} + v_{zz}), \quad (2)$$

$$u w_x + v w_y + w w_z = -\rho^{-1} p_z + \mu(w_{xx} + w_{yy} + w_{zz}), \quad (3)$$

and the continuity equation

$$u_x + v_y + w_z = 0, \quad (4)$$

where subscripts denote partial differentiation, ρ is the density, p the pressure, μ the absolute viscosity; and u , v , w are dimensional velocity components in the directions of the streamwise coordinate, x , the spanwise coordinate, y , and the normal to the plate, z , respectively (see Figure 1 for coordinate system). Equations (1)-(4) are sufficient for describing the complete protuberance flow field, but would be very difficult to apply in practice. If we concentrate, instead, on the downstream flow field, then we suspect that if we initialize the calculations "far enough" downstream, we can use the boundary-layer or boundary-region equations to describe the flow field.

The 3-D boundary layer equations can be derived from Equations (1)-(4) through either an order-of-magnitude analysis, or by formally applying limit processes at high Reynolds numbers. The resulting equations, in non-dimensional form, are

$$U U_x + V U_y + W U_z = -P_x + U_{zz} \quad (5)$$

$$U V_x + V V_y + W V_z = -P_y + V_{zz} \quad (6)$$

$$U_x + V_y + W_z = 0 \quad (7)$$

where the non-dimensional variables are defined by

$$X = x/L, \quad Y = y/L, \quad U = u/u_\infty, \quad V = v/u_\infty \quad (8)$$

$$Z = z \text{Re}^{1/2}/L, \quad W = w \text{Re}^{1/2}/u_\infty, \quad P = p/(\rho u_\infty^2) \quad (9)$$

with

$$\text{Re} = \rho u_\infty L / \mu. \quad (10)$$

The freestream velocity is u_∞ and L represents a reference length, taken to be 1 cm in the present problem.

The 3-D boundary-region equations, on the other hand, cannot be formally derived from Equations (1)-(4), to the best of our knowledge. Rather, they represent an ad hoc approximation that has been used in some other investigations to treat problems where crossflow diffusion effects were not

negligible. They were first used by Kemp⁴ for the flow over two intersecting flat plates, the corner problem, and have been employed extensively by many authors for that problem. The boundary-region equations can be derived, using familiar limiting processes, for the corner problem, but not for the present problem or many others to which they have been applied. Therefore, to account for the expected crossflow diffusion effects, we adopt the boundary-region approximation expressed by

$$U U_X + V U_Y + W U_Z = -P_X + U_{ZZ} + \text{Re}^{-1} U_{YY} \quad (11)$$

$$U V_X + V V_Y + W V_Z = -P_Y + V_{ZZ} + \text{Re}^{-1} V_{YY} \quad (12)$$

$$U_X + V_Y + W_Z = 0, \quad (13)$$

where the unusual form of the diffusion terms on the right hand side results from the way in which z is non-dimensionalized.

We can write a single set of equations that expresses both the boundary-layer and boundary-region approximations

$$U U_X + V U_Y + W U_Z = -P_X + \epsilon \text{Re}^{-1} U_{YY} + U_{ZZ} \quad (14)$$

$$U V_X + V V_Y + W V_Z = -P_Y - \epsilon \text{Re}^{-1} V_{YY} + V_{ZZ} \quad (15)$$

$$U_X + V_Y + W_Z = 0, \quad (16)$$

where $\epsilon = 0$ gives the 3-D boundary-layer equations and $\epsilon = 1$ gives the 3-D boundary-region equations. The boundary-region approximation includes one additional crossflow diffusion term in each momentum equation that is neglected in the 3-D boundary-layer theory. Both approximations neglect the normal momentum equation, assuming that normal pressure gradient $P_Z = 0$; model equations with $P_Z \neq 0$ could also be developed. The boundary conditions applicable to Equations (14)-(16) will be described in Section V. When the external flow is uniform, as is assumed here, $P_X = P_Y = 0$.

III. TANI TEST PROBLEM

We have attempted to apply Equations (14)-(16) to describe the flow field downstream of a typical small cylindrical protuberance. Experimental hot wire anemometry measurements taken by Tani, et al.³ establish the presence and persistence of streamwise vortices in the downstream flow field for various

4. Kemp, N., "The Laminar Three-Dimensional Boundary Layer and a Study of the Flow Past a Side Edge", M.Ae.S. Thesis, Cornell University, 1951.

free stream conditions. The test problem treated here corresponds to Tani's experimental arrangement with a cylindrical protuberance ($k = 0.25\text{cm}$), where k is the protuberance height, mounted normal to a flat plate placed in a wind tunnel; see Figure 1. The protuberance height is equal to its diameter and the freestream velocity is 520cm/s , with a free stream turbulence level of approximately 0.2%. The protuberance leading edge is located at $x_k = 60\text{ cm}$. For these conditions the protuberance height is approximately 39% of the local boundary-layer thickness, δ , at $x = x_k$, based on the 99%-velocity thickness. The Reynolds number based on x_k , with $\nu = \mu/\rho = 0.15\text{cm}^2/\text{s}$ is

$$\text{Re}_{x_k} = u_\infty x_k / \nu = 2.08 \times 10^5$$

and the roughness Reynolds number is

$$\text{Re}_k = 550,$$

defined in terms of the protuberance height and the local undisturbed velocity at $x = x_k$, $z = k$.

Tani took hot wire surveys of the protuberance flow field at various x to study the manner in which the streamwise vortices redistribute momentum in the boundary layer and affect transition. His measurements taken at $(x-x_k)/k = 10$ are used in the present study to construct a plane of data for "initializing" the marching schemes used to solve Equations (14)-(16). From the limited data taken by Tani, distributions of velocity components which fit these data must be constructed in order to generate the initial plane flow. This is accomplished by combining the available data with theoretical considerations, so that U , V , and W are prescribed everywhere at $(x-x_k)/k = 10$. This process is described in the next section.

In addition to velocity fields, Reference 3 presents data for measurements of the flow perturbation caused by the protuberance and the spacing of the vortices for downstream distance $(x-x_k)/k = 244$; these data are used to test the calculations. The transition process, which starts at $x = x_t$, begins further downstream; from Reference 3, $(x_t-x_k)/k \approx 4500$.

IV. INITIAL PLANE OF DATA

The experimental data³ upon which the velocities in the initial plane, $x_1 = x_k + 10k$, are based are shown in Figure 2. The u and v distributions are consistent with two vortices, symmetrical about $y = 0$, but are insufficient to characterize the entire flow field. They must be supplemented with theoretical considerations and assumptions. The deviation of the fitted values from

the actual velocity field might be large for some y and z because of the paucity of the data.

Figures 2a and 2b furnish data at only three values of z , whereas values of U_1-U_2 are given in Figure 2c for many z values. The curves in these figures are from Reference 3, representing the authors' smoothing of the data. Figure 2c, together with Figure 6 of Reference 3, shows that the shape of the $U(Y)$ curves is the same for all Z ; only the magnitude changes. Three quantities are defined graphically in Figure 2a: U_1 and U_2 are the maximum and minimum values, respectively, of U off the plane of symmetry at fixed values of Z ; $s/2$ is the maximum value of Y at which $U = \frac{1}{2}(U_1 + U_2)$ and is thus a measure of the spacing of the two legs of the horseshoe vortex. A measure of the perturbation due to the horseshoe vortex is $U_1 - U_2$; for Figure 2 it is approximately 20% of the local Blasius value of U .

The fits for U and V in the initial plane are:

$$U_I = U_B + 1.961 [1.519 \eta f_0'' (1.519 \eta)] [U_T(Y) - U_T(2.5)] \quad (17)$$

$$V_I = -1.217 \eta U_I F_2 (1.558 \eta) \tan 3_T (Y), \quad (18)$$

where

$$\eta = Z/(2 x_I)^{1/2} = [u_\infty/(2\nu x_I)^{1/2}]z, \quad (19)$$

$$U_B = f_0' (\eta) \quad (20)$$

are the Blasius variables. The process which led to these fitting functions is described below.

The functions $f_0' (\eta)$, $\eta f_0'' (\eta)$, and $F_2 (\eta)$ are tabulated in Appendix A. These are obtained by solving

$$\begin{aligned} f_0''' (\eta) + f_0 f_0'' &= 0 \\ F_2'' + f_0 F_2' + 3.3873 f_0' F_2 &= 0, \end{aligned} \quad (21)$$

where $f_0 (0) = f_0' (0) = 0$; $f_0' (\infty) = 1$

$F_2 (0) = F_2 (\infty) = 0$.

F_2 is an eigenfunction occurring in the boundary-layer perturbation analysis of Fox and Libby⁵.

The functions $U_T(Y)$ and $\beta_T(Y)$ are obtained by dividing the Y -axis into segments and empirically fitting the data of Figure 2 in each segment with a 3rd-order polynomial, with continuity of the functions and first derivatives required at tie-points.

$$\begin{aligned} U_T(Y) &= a_0 + a_1 Y + a_2 Y^2 + a_3 Y^3 \\ \beta_T(Y) &= b_0 + b_1 Y + b_2 Y^2 + b_3 Y^3 \quad (\text{in degrees}), \end{aligned} \quad (22)$$

where β_T is fitted at $z = 0.18$ cm. The imposed symmetry requires that we need to consider only $Y \geq 0$. Five segments were used here. The a_j and b_j coefficients and tie-points are provided in Appendix B. Regrettably, the boundary-region approximation was not under consideration when the cubic spline fits were made for U_T and β_T ; consequently U_{YY} and V_{YY} in Eqs. (14) and (15) are discontinuous at the tie-points.

The following process was used to arrive at Eqs. (17) and (18). We imposed the plausible assumption that as either $Y \rightarrow \infty$ or $Z \rightarrow \infty$, U approaches Blasius flow and V approaches zero. In Eq. (17) the Blasius U is reached at $Y = 2.5$. The function $n f_0''(n)$ has the same shape and limits as the U_1-U_2 data in Figure 2c, which measure the amplitude of perturbation to Blasius flow. The two constants in Eq. (17) were obtained by imposing two conditions: (i) U should agree with Tani's measurement at $y = 0.30$ cm and $z = 0.25$ cm (Figure 2a), and (ii) the peak of the $n f_0''(n)$ curve should occur at $z = 0.24$ cm, the peak of the data in Figure 2c. As for Eq. (18), Figure 2b indicates a reversal in phase of the β versus y profiles between $z = 0.18$ cm and $z = 0.33$ cm; the function $F_2(n)$ provides this feature. The two constants in Eq. (18) were obtained by forcing the analytical expression for V_I to agree with the data at $y = 0.30$ cm, $z = 0.18$ cm, and $y = 0.30$ cm, $z = 0.33$ cm.

Results of the fitting are compared with Tani's measurements in Figure 3, which shows spanwise distributions, and Figure 4, which shows variation normal to the plate. In Figure 3b only the data for $y > 0$ and $z = 0.18$ cm were used to determine the constants, and the deviation between these data and the fitted curve is relatively small. Although the deviation for $y < 0$ is relatively large, it is apparent that the scatter in the data is also large, e.g., the data for β is not an odd function of y . In fitting the data, however, we required the symmetry conditions to be satisfied.

5. Fox, H., and Libby, P.A., "Some Perturbation Solutions in Laminar Boundary Layer Theory. Part 2. The Energy Equation", J. Fluid Mech., Vol. 19, 1964, pp. 433-451.

The vertical component, W , is found from U and V by subtracting Eq. (14) from $[U \text{ times Eq. (16)}]$, then separating out the resulting $\partial(W/U)/\partial Z$ term and integrating:

$$W = U \int_0^Z \{ [P_X - UV_Y + VU_Y - (\epsilon \text{ Re}^{-1} U_{YY} - U_{ZZ})] / U^2 \} dZ. \quad (23)$$

A similar expression can be derived using Eqs. (15) and (16). For uniform external flow, $P_X = 0$. The Y - and Z - derivatives are evaluated by finite differences at the mesh points in the Y, Z plane with 3-point formulas, and W is obtained by numerical integration of the right-hand side of Eq. (23). The integrand, J , of Eq. (23) is indeterminate but finite at $Z = 0$, so that at the first level of mesh points off the plate,

$$W(Z=\Delta Z) \approx \frac{1}{2} \Delta Z U(\Delta Z) J(\Delta Z/2).$$

The computation fails if $U = 0$ off the plate; however, this has never occurred. The boundary-layer and boundary-region approximations yield different distributions because of the absence or presence of the $\text{Re}^{-1} U_{YY}$ term.

In Figure 5 the velocity vectors are shown projected into the initial plane (as viewed looking downstream from the protuberance). The U - and V -components are identical in both approximations, but the W -components are different. A mesh point lies at the tail of each velocity vector. The boundary-layer approximation leads to two counter-rotating vortices on each side of the plane of symmetry. In the boundary-region approximation, there is one large vortex and possibly several smaller vortices that are not clearly defined. One noticeable difference occurs at the plane of symmetry, $Y = 0$; in the boundary-region case the flow is toward the plate, while in the boundary-layer case the flow is away from the plate.

The differences between the two flow patterns in Figure 5 suggest that U_{YY} , and therefore, V_{YY} are not negligible for this vortical flow. Figure 6 compares u_{yy} with u_{zz} at $Z = 1.0$. (Since these two terms are dimensional, they may be compared directly, no stretching factor being involved.) This figure shows that u_{yy} is 8 times as large as u_{zz} in some parts of the initial plane. Thus the boundary-layer approximation is violated in this plane because it requires $u_{yy} \ll u_{zz}$.

That the boundary-layer approximation may be violated can be anticipated from the large gradients, e.g., U_y shown in the data in Figure 2a. The question arises whether or not a boundary layer calculation should be attempted. It was decided to do this on the possibility that the large gradients would be smoothed out and that the downstream flow could be calculated.

V. NUMERICAL PROCEDURE AND BOUNDARY CONDITIONS

The equations were solved using the predictor-corrector multiple-iteration (PCMI) method, which has two advantages. It can be used for both sets of equations, and the truncation error is uniformly second order. One

alternative procedure for the boundary layer equations is discussed later.

The numerical solution to Eqs. (14)-(16) is obtained by marching downstream (X-direction) from the initial data plane. Symmetry boundary conditions

$$\partial U / \partial Y = V = \partial W / \partial Y = 0 \quad (24)$$

are applied at $Y = 0$ and Blasius flow is prescribed at $Y = 2.5$. The free-stream velocity components ($U = 1$ and $V = 0$) are prescribed at $Z = 100$. The numerical procedure is based on a predictor-corrector multiple-iteration (PCMI) technique developed by Rubin and Lin⁶. The procedure is implicit in the Z-direction. All flow gradients in the Y-direction are approximated by prediction and subsequent correction using an iterative approach, which gives a more accurate simulation of the nonlinear coupling between equations. The solution is obtained for each grid column by inverting a tridiagonal matrix.

Appendix C gives the set of difference equations used in this study. The truncation errors for interior points are of $O(\Delta x^2, \Delta Y^2, \Delta Z^2)$. The PCMI procedure solves the momentum difference equations for U^{m+1} and V^{m+1} , using the m-iterate values to form the coefficients of the nonlinear terms and approximate Y-derivatives, where m denotes the iteration level. The continuity equation is then solved for W^{m+1} .

For the predictor step, or first iteration, terms in Eqs. (C-1)-(C-10) with superscript zero are approximated by a Taylor series to $O(\Delta X^2)$:

$$F_{i+1,j,k}^0 = F_{i,j,k} + (F_{i,j,k} - F_{i-1,j,k}) (X_{i+1} - X_i) / (X_i - X_{i-1}). \quad (25)$$

During the first X-step an extrapolation of $O(\Delta X)$ is used. After extrapolating guesses for U^0 , V^0 and W^0 at X_{i+1} , Eqs. (C-1) and (C-6) are solved to give U^1 and V^1 . The calculations start at the plane of symmetry and work outward in Y. The (m+1)-iterate values are used to approximate derivatives in the Y-direction as soon as they become available; see Eqs. (C-5) and (C-10). Next Eq. (C-11) is solved for W^1 , starting at $Y = Z = 0$ and sweeping in Z and then Y. This completes the first iteration cycle. Subsequent iterations allow the nonlinear terms to be corrected and the symmetry plane boundary conditions to be satisfied.

6. Rubin, S.G., and Lin, T.C., "A Numerical Method for Three-Dimensional Viscous Flow: Application to the Hypersonic Leading Edge", J. Comp. Phys., Vol. 9, 1972, pp. 339-364.

Numerical studies were performed to determine the number of iterations required to give satisfactory convergence of the solution. These indicate that three iterations assure convergence of U , V , and W to at least four decimal places, which we consider to be sufficiently accurate. Consequently at least three iterations were used for subsequent calculations. The number of iterations used varied with ΔX , which ranged from 0.010 near the initial data plane to 0.250 at the last downstream station. The value of ΔX was adjusted during the calculations to satisfy the linear stability criterion

$$\Delta X < \Delta Y |U/V|. \quad (26)$$

Eq. (26) is based on a linear stability analysis for interior points, including the effect of multiple iteration⁶. A 41×41 ($Y \times Z$) grid was used for each $X = \text{constant}$ plane with $\Delta Y = 0.025$ for $0 < Y < 0.5$, $\Delta Y = 0.100$ for $0.5 < Y < 2.5$ and $\Delta Z = 2.50$ for $0 < Z < 100$. The variable spacing in Y was adopted to help resolve the large crossflow gradients indicated in Figure 2 for $0 < Y < 0.5$.

Special second-order accurate difference approximations for $\partial F/\partial Y$ and $\partial^2 F/\partial Y^2$ are employed at $Y = 0.5$ due to the unequal mesh spacing, where F represents U or V .

VI. RESULTS AND COMPARISON WITH EXPERIMENT

Computations were carried out for the vortical flow downstream of the protuberance using both the boundary-layer and boundary-region approximations. The boundary-layer calculation failed when it predicted streamwise flow reversal; the boundary-region calculation, on the other hand, was carried to 244 protuberance heights downstream (Tani's last station) without encountering computational difficulties.

Crossflow velocity vector plots at $(x - x_k)/k = 16$ are presented in Figure 7, which shows the initial stages of the breakdown of the boundary-layer calculation. Large gradients, W_Y , are predicted at $Y = 0.025$ and 0.3 which were not present in the initial plane. As the calculation proceeds, they are not smoothed out, due to lack of crossflow diffusion. The positive W along the plane of symmetry, present on the initial plane, is still in evidence. At $x = x_k + 20 k$ the W -component is larger and the U -component reverses direction, as if streamwise separation had occurred. Since there is no pressure gradient in this flow, the usual cause of separation, an adverse pressure gradient, cannot be invoked. We only note that (i) for both the initial plane and for $(x-x_k)/k = 16$, $W > 0$ in the neighborhood of $Y = 0$, and (ii) $U_Z > 0$ up to the point of flow reversal; thus the term WU_Z could play the role of an adverse pressure gradient. At any rate the boundary-layer calculation cannot proceed beyond $x = x_k + 20 k$.

For the boundary-region calculation the crossflow velocity vector plot in Figure 7 shows that some anomalies that existed in the initial plane, caused by discontinuities in second derivatives with respect to Y , have been smoothed out. The presence of the main vortex is clearly seen. In contrast to the

boundary layer results, $W < 0$ near $Y = 0$ at this plane as it was in the initial plane, and the gradients are smaller, the largest W_y for the boundary region case being 20% of that for the boundary layer case. These differences between the results of the two approximations are felt to be related to the success of the boundary region calculation.

Figure 8 shows the downstream variation of the maximum value of the streamwise vorticity, $\zeta_x (= \partial W / \partial Y - \partial V / \partial Z)$, evaluated at the wall. This is a measure of the strength of the horseshoe vortex. Results from the boundary-layer calculation are terminated where it breaks down. The streamwise vorticity from the boundary-region calculation is essentially zero at about 150 protuberance heights downstream.

With regard to crossflow velocity, the boundary-region calculation predicts that the flow inclination at $(x - x_k)/k = 244$ is less than 0.2° . Tani could not detect any crossflow velocity component at 244 protuberance heights downstream. In fact, 0.2° is within scatter of his data.

Figure 9 shows the streamwise variation of the horseshoe vortex spacing, s . The variation predicted by the boundary-region approximation is seen to agree qualitatively with Tani's measurements. At the last downstream station the predicted spacing is about 25% larger than the measurement. The trend of the calculated s is the same as that of the data.

Figure 10 shows the variation of the maximum velocity difference, $(U_1 - U_2)_{\max}$. The quantity $U_1 - U_2$ is evaluated in each crossflow plane and the largest value, $(U_1 - U_2)_{\max}$ is plotted. The boundary-region calculation predicts that the perturbation in U grows to ~ 0.19 at $x = x_k + 25k$ and then begins to decay. The calculated perturbation decays faster than the measured value up to $(x - x_k)/k = 200$; thereafter the calculated value is essentially constant and is 38% of the experimental value at 244 protuberance heights downstream. Note that the perturbation in U is still present at $(x - x_k)/k = 244$, although the crossflow velocity has decayed to nearly zero and the maximum streamwise vorticity at the wall is already zero. These conclusions apply also to the experimental data.

The failure of the boundary layer calculation would seem to be related to the lack of a mechanism for smoothing out or diffusing the large crossflow gradients in the initial data. However, care must be taken in drawing conclusions from the results of these numerical solutions because the failure of the PCMI boundary-layer calculation may be a product of the numerical scheme and/or the inadequacy of the boundary layer model itself. An indication might be obtained by trying other schemes. Rather than try schemes similar to the PCMI, which would probably fail in the same way, we used a scheme that adds support to the statement made in the first sentence of this paragraph. The

scheme chosen was the one in Reference 7, called Scheme D, on the basis of zone-of-dependence sensitivity. For details see Reference 7. The truncation errors for this scheme are $O(\Delta X, \Delta Y^2, \Delta Z^2, \Delta Y^2/\Delta X)$. In contrast with the PCMI truncation error, this scheme is only first order in ΔX and has the additional error $\Delta Y^2/\Delta X$. The latter arises from artificial diffusion introduced by the X-difference equation. Using standard truncation error analysis techniques, it can be shown that two artificial viscosity terms, αU_{YY} and αV_{YY} , where $\alpha = \Delta Y^2/\Delta X$, are introduced into the finite-difference equations⁸. These two artificial viscosity terms have the same form as the crossflow diffusion terms in the boundary-region approximation. These terms have the effect of smoothing out the initial large crossflow gradients, and the calculation proceeds beyond the point where the boundary layer PCMI calculation failed. Apparently the Scheme D boundary-layer difference equations behave in a manner similar to the boundary-region approximation. By increasing ΔX from 0.01 at the initial plane to 0.50 far downstream, the calculation proceeded to $X = 244$. However, the results compared poorly with the data. Figure 11 shows the values of s from this scheme together with the boundary-region result. The divergence between the results, as X increases, may be caused by the fact that α is 50 times smaller downstream than near the initial plane, and hence the artificial diffusion is small, or perhaps because ΔX is 50 times larger than near the initial plane and thus produces unacceptable truncation errors. The conclusion is that this boundary-layer calculation fails but in a different sense from the PCMI failure.

VII. CONCLUSIONS

In this study we have shown that the three-dimensional boundary-region approximation can be successfully used to describe the flow downstream of a cylindrical protuberance immersed in a laminar flat plate boundary layer. The persistence of the streamwise vorticity downstream of the obstacle is predicted in agreement with experimental observations. We find that the streamwise vorticity persists more than 100 protuberance heights downstream and that the initial perturbations in U decay more slowly than the vorticity. Significant perturbations in U are still present 244 protuberance heights downstream of the obstacle in the boundary-region calculation. This is quite remarkable

7. Kitchens Jr., C.W., Sedney, R., and Gerber, N., "The Role of the Zone of Dependence Concept in Three-Dimensional Boundary-Layer Calculations", U.S. Army Ballistic Research Laboratory/ARRADCOM Report No. 1821, Aberdeen Proving Ground, MD, August 1975. AD A016896.

8. Roache, P.J., "On Artificial Viscosity", J. Comp. Phys., Vol. 10, October 1972, pp. 169-184.

considering that we have marched more than a hundred boundary-layer thicknesses downstream to reach this position. The experimental data show the same qualitative trend.

The three-dimensional boundary-layer approximation, on the other hand, is not successful in describing the flow field downstream of the protuberance. It fails due to the large crossflow gradients present in the protuberance flow field. These gradients lead to the reversal of the streamwise velocity component, U , during the marching process.

It is expected that the quantitative agreement between the boundary-region calculations and Tani's experimental data would be improved if the initial data were fitted using 4th-order (or higher) polynomials so that U_{yy} and V_{yy} were continuous. Accuracy could be further improved by using smaller grid sizes during the marching process. Unfortunately, it is not possible to quantify the expected improvement. These refinements may not be warranted in the present problem, considering the sparse experimental data available for constructing initial data.

Whether or not the boundary-region approximation employed here is the most adequate model for this flow field cannot be established unequivocally by this investigation. In our version we assumed that the normal pressure gradient, $\partial P/\partial Z$, is zero. It is possible that dropping this assumption would improve the quantitative agreement with experiment.

REFERENCES

1. Morkovin, M.V. "Observations on Streamwise Vortices in Laminar and Turbulent Boundary Layers", NASA Contractor Report 159061, April 1979.
2. Sedney, R., "A Survey of the Effects of Small Protuberances on Boundary-Layer Flows", AIAA Journal, Vol. 11, No. 6, June 1973, pp. 782-792.
3. Tani, I., Komoda, H., and Komatsu, Y., "Boundary-Layer Transition by Isolated Roughness", Aeronautical Research Institute Report No. 375, University of Tokyo, November 1962.
4. Kemp, N., "The Laminar Three-Dimensional Boundary Layer and a Study of the Flow Past a Side Edge", M.Ae.S. Thesis, Cornell University, 1951.
5. Fox, H., and Libby, P.A., "Some Perturbation Solutions in Laminar Boundary Layer Theory. Part 2. The Energy Equation", J. Fluid Mech., Vol. 19, 1964, pp. 433-451.
6. Rubin, S.G., and Lin, T.C., "A Numerical Method for Three-Dimensional Viscous Flow: Application to the Hypersonic Leading Edge", J. Comp. Phys., Vol. 9, 1972, pp. 339-364.
7. Kitchens Jr., C.W., Sedney, R., and Gerber, N. "The Role of the Zone of Dependence Concept in Three-Dimensional Boundary-Layer Calculations", U.S. Army Ballistic Research Laboratory/ARRADCOM Report No. 1821, Aberdeen Proving Ground, MD, August 1975. AD A016896.
8. Roache, P.J., "On Artificial Viscosity", J. Comp. Phys., Vol. 10, October 1972, pp. 169-184.

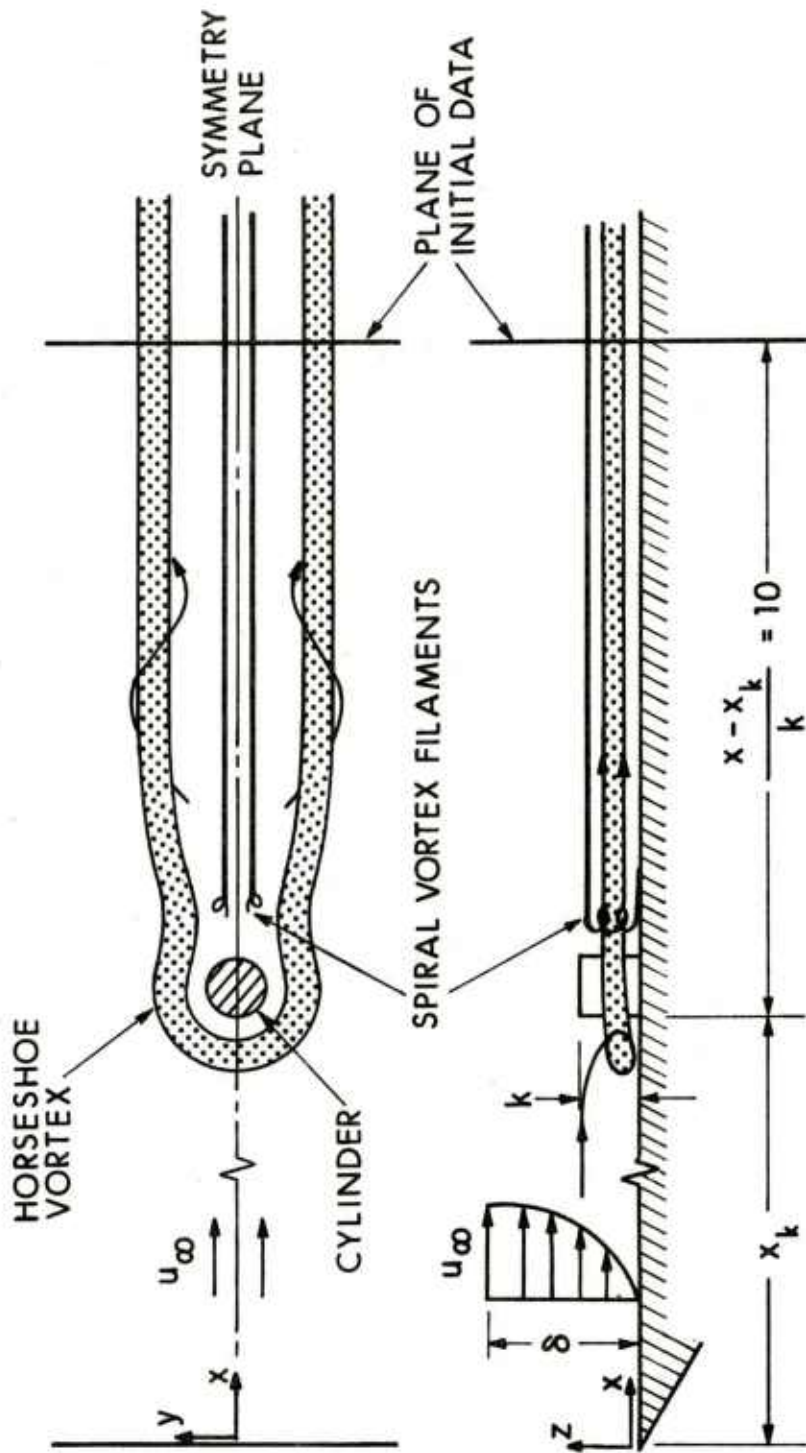


Figure 1. Sketch of Protuberance in Boundary Layer in Tani Experiment ($k/\delta = 0.39$, $Re_{x_k} = 2.08 \times 10^5$, $Re_k = 550$)

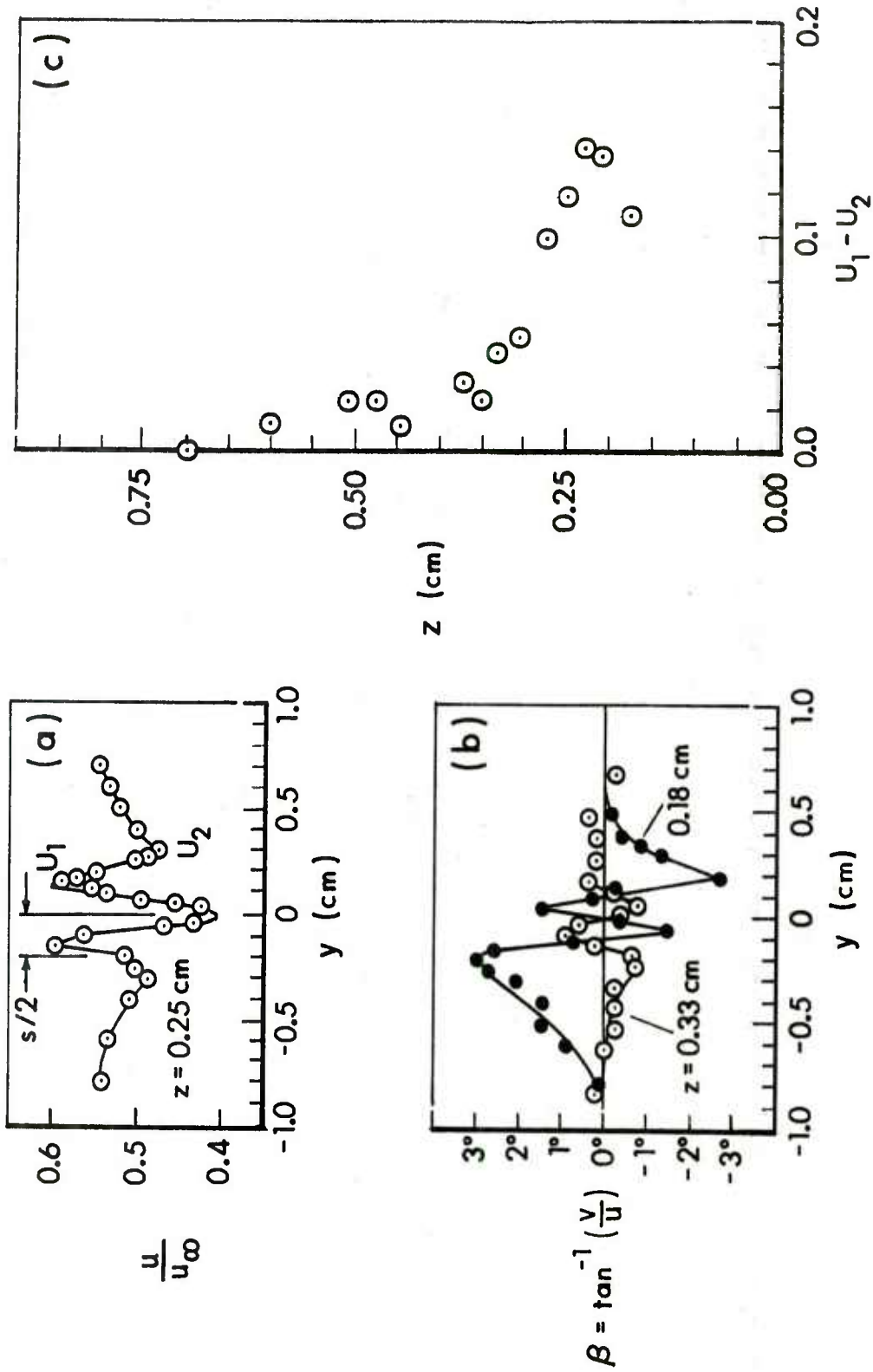


Figure 2. Measured Spanwise Distribution at $x_I = x_k + 10k$ of (a) Streamwise Velocity Component and (b) Flow Inclination in the x,y Plane at Two Heights; (c) Experimental Distribution Across Boundary Layer of Peak-Valley Velocity Difference ($U_1 - U_2$)

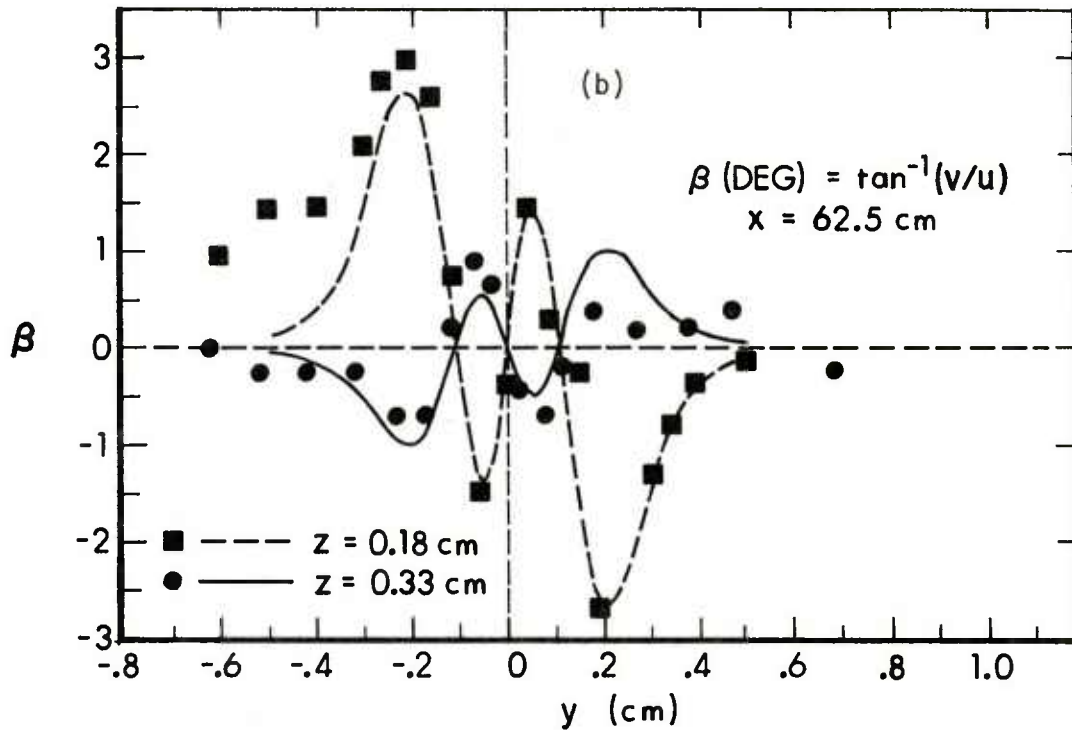
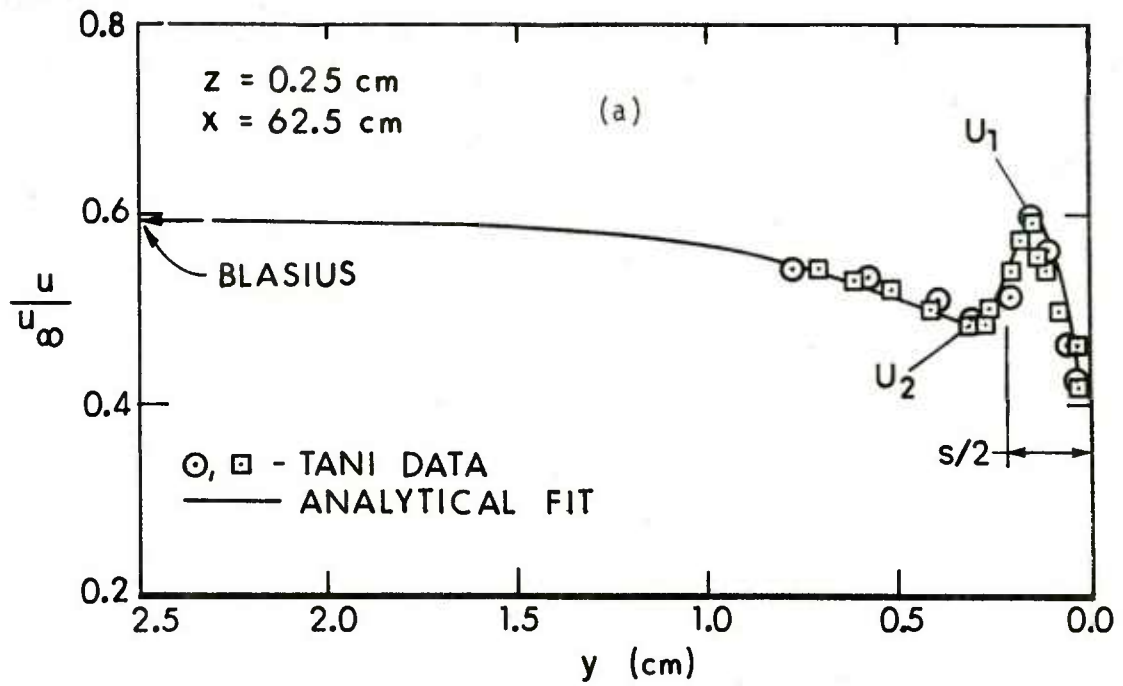


Figure 3. Analytical Spanwise Distributions of (a) u/u_∞ and (b) $\beta \equiv \tan^{-1}(v/u)$, Eqs. (17) and (18), at Fixed Heights in the Initial Data Plane, and Comparison with Tani Data.

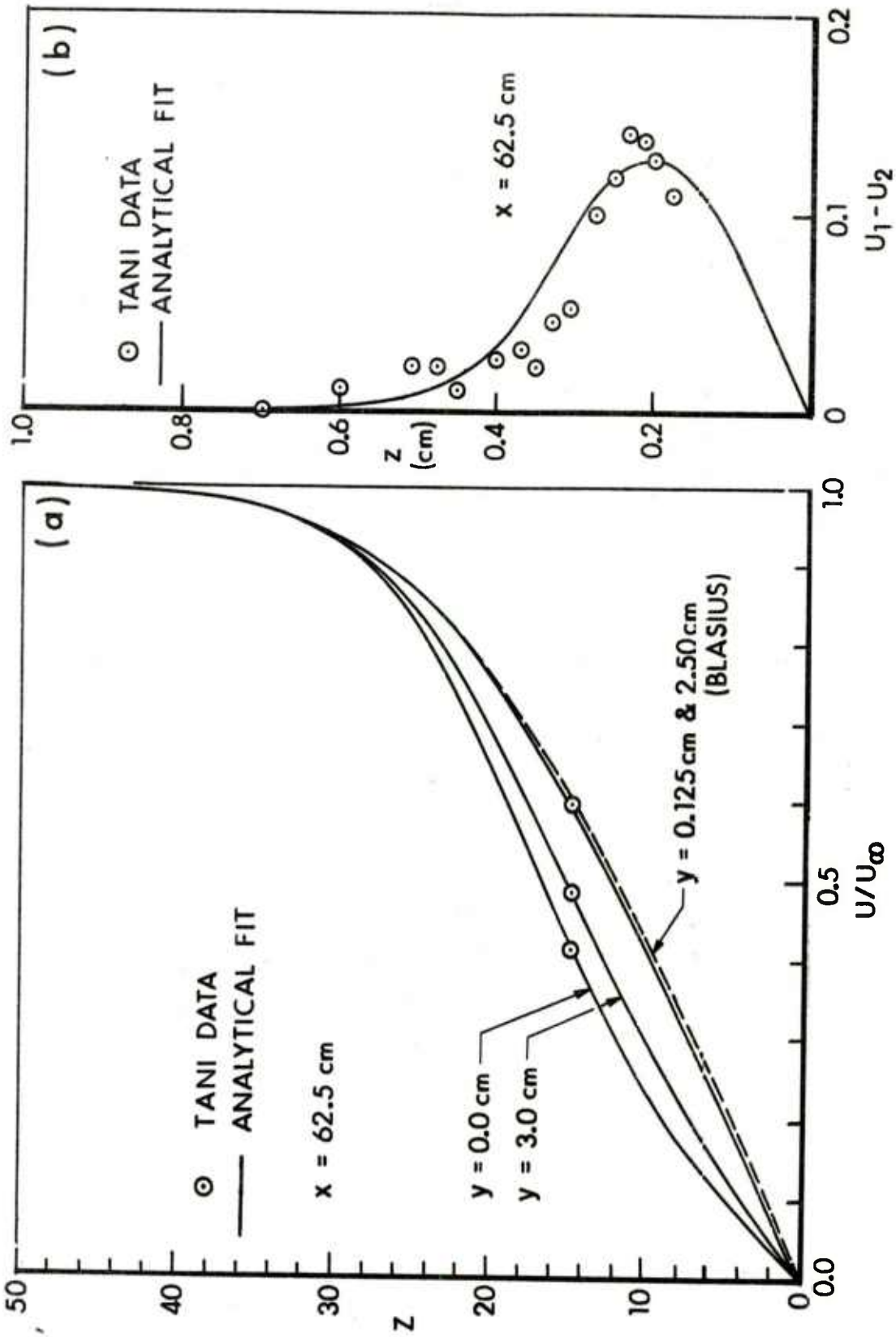
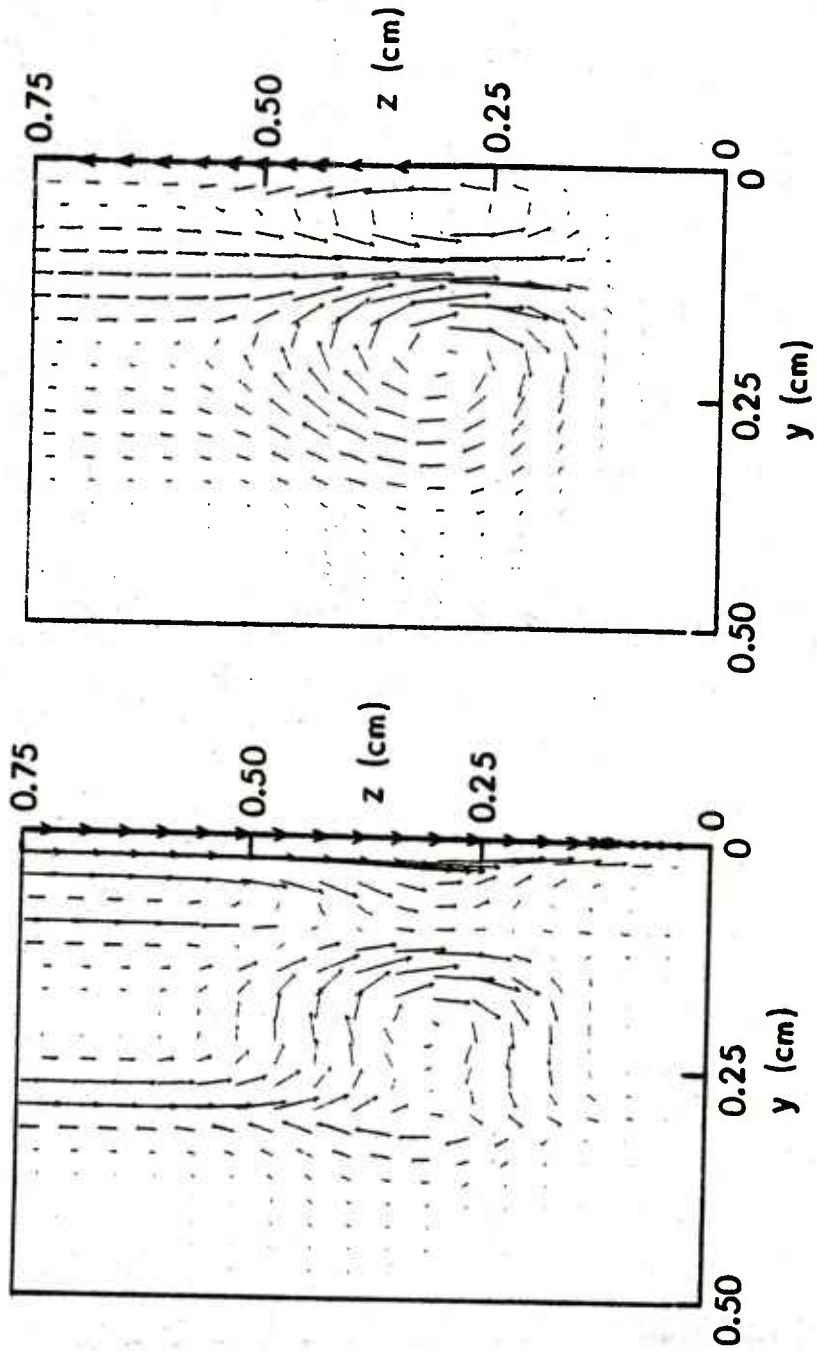


Figure 4. Analytical Distributions of (a) u/u_∞ and (b) $U_1 - U_2$ Through the Boundary Layer in the Initial Data Plane, and Comparison with Tani Data.

$$\frac{x - x_k}{k} = 10$$



BOUNDARY REGION

BOUNDARY LAYER

Figure 5. Crossflow Plane (y,z) Velocity Vector Projections in Initial Data Plane at $x = x_k + 10k$

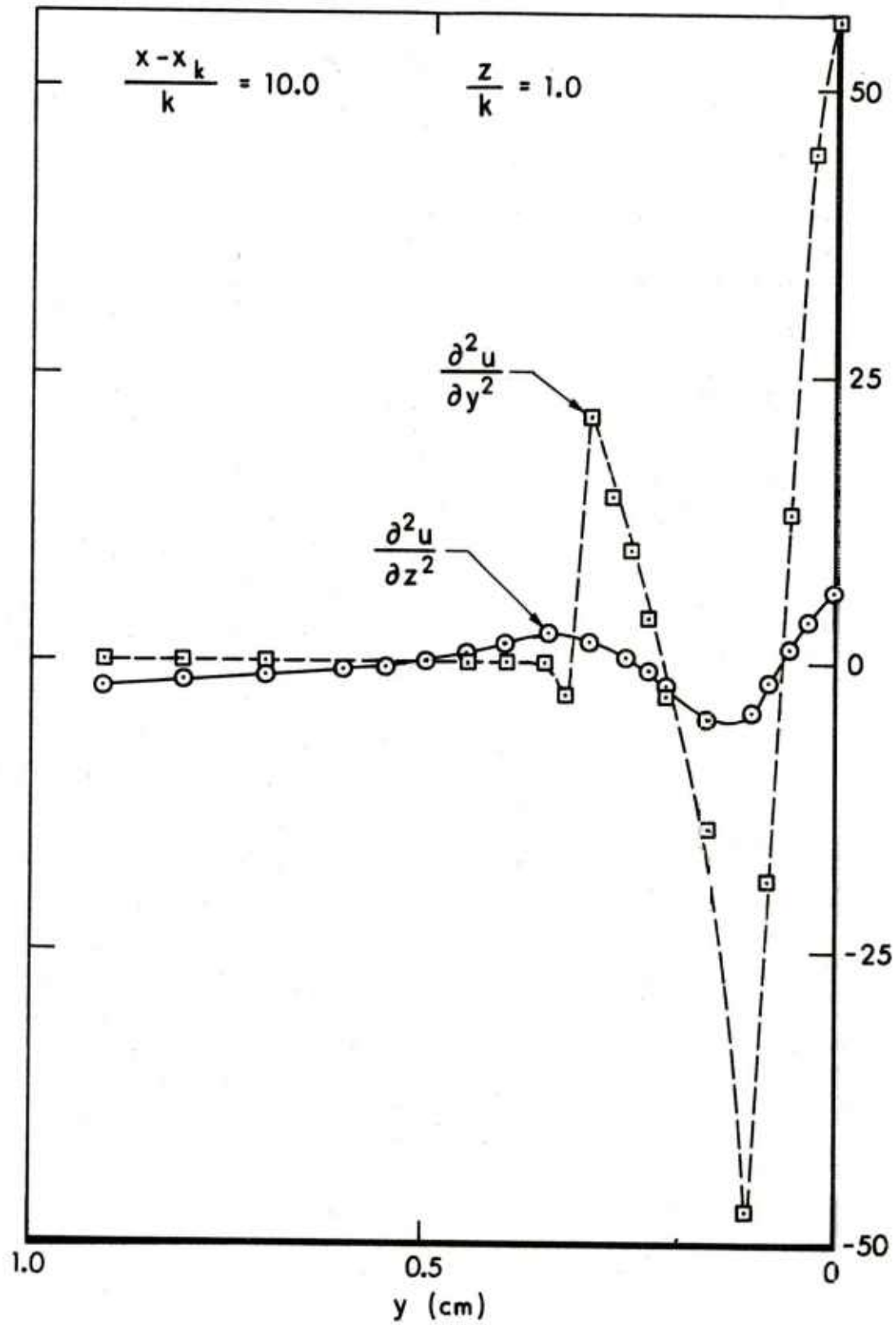
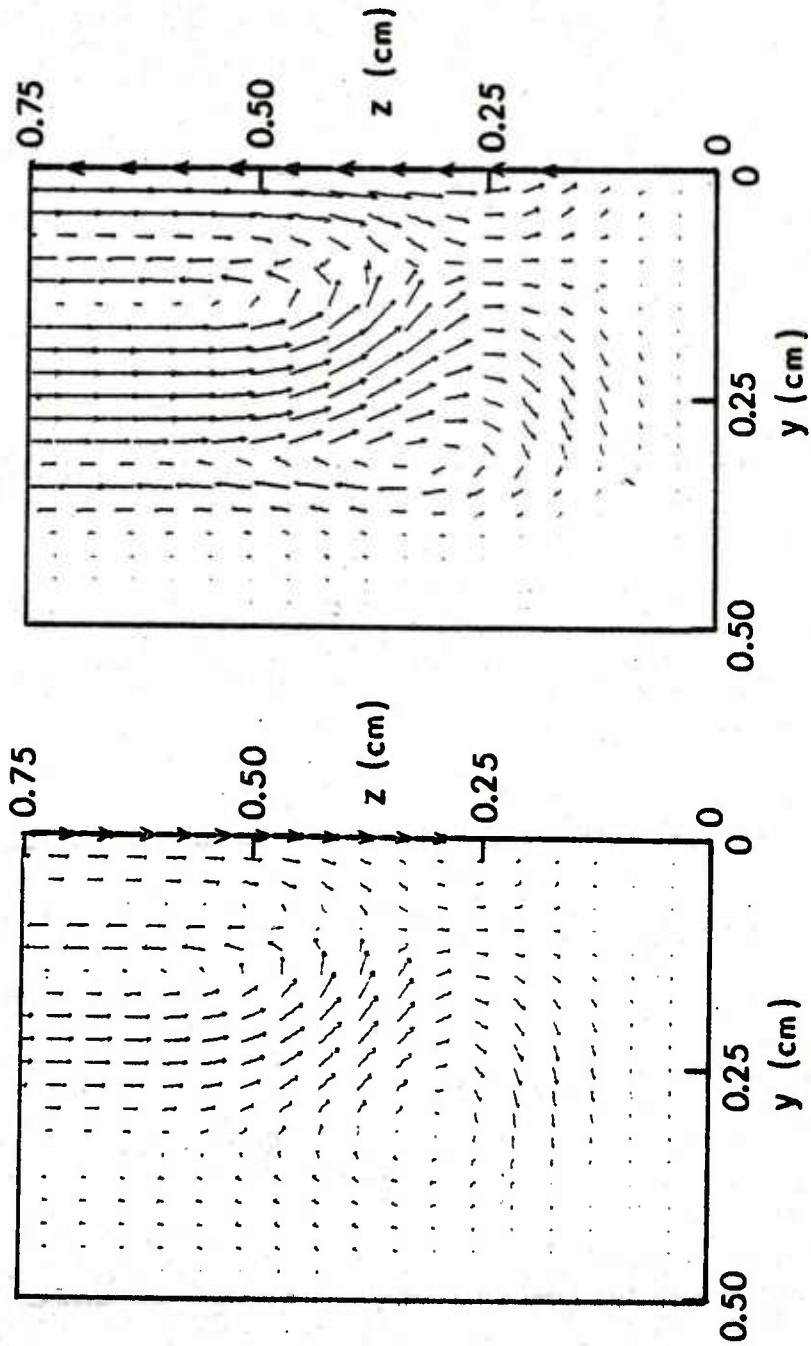


Figure 6. Spanwise Distribution of Second-Derivatives of Streamwise Velocity Component in Initial Data Plane

$$\frac{x - x_k}{k} = 16$$



BOUNDARY REGION

BOUNDARY LAYER

Figure 7. Crossflow Plane (y, z) Velocity Vector Projections at $x = x_k + 16k$

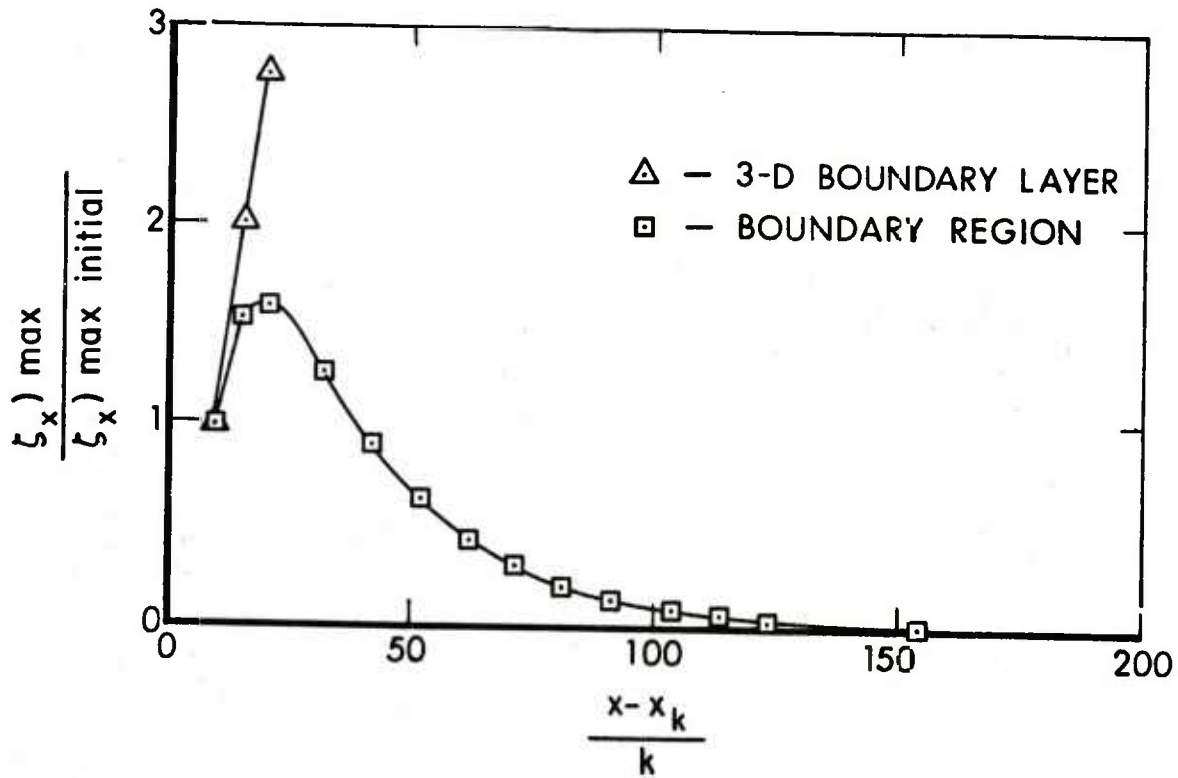


Figure 8. Streamwise Variation of Maximum Vorticity at Wall

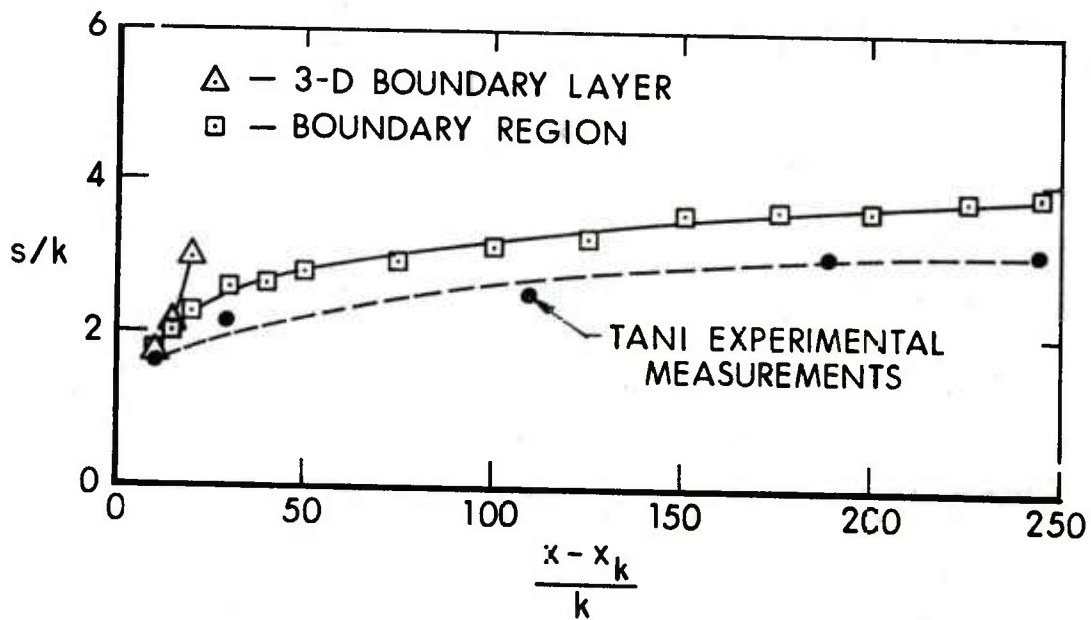


Figure 9. Streamwise Variation of Horseshoe Vortex Spacing

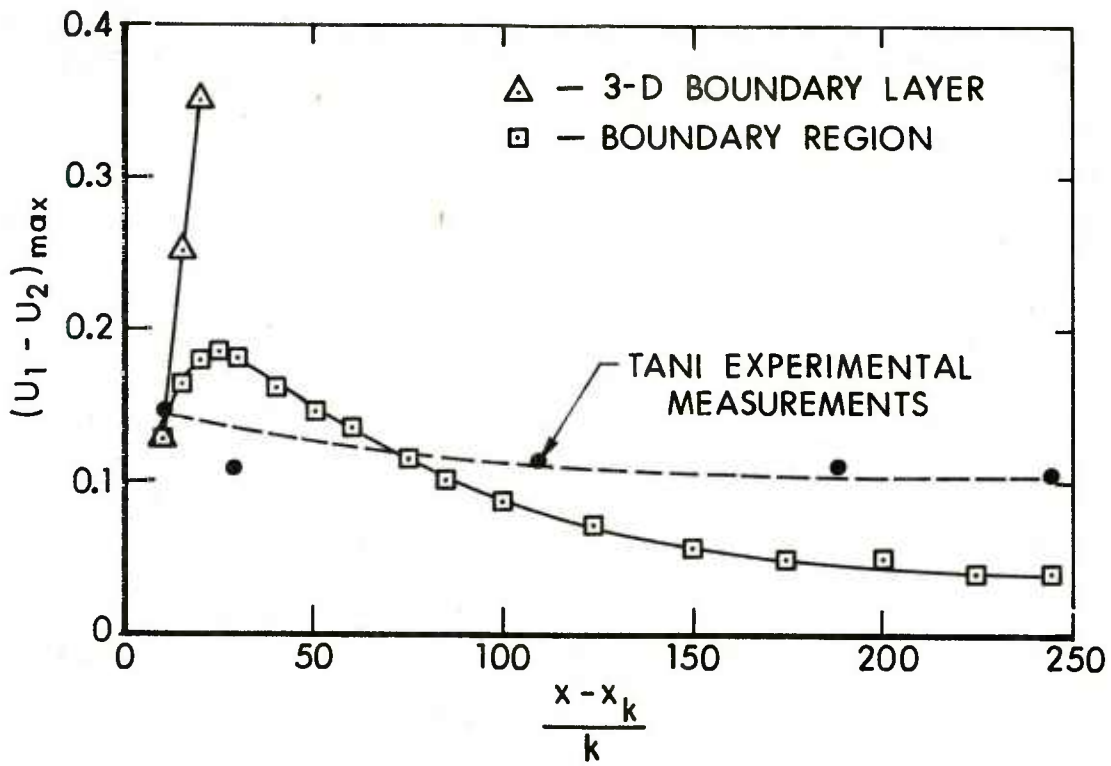


Figure 10. Streamwise Variation of Maximum Peak-Valley Velocity Difference Induced by Horseshoe Vortex

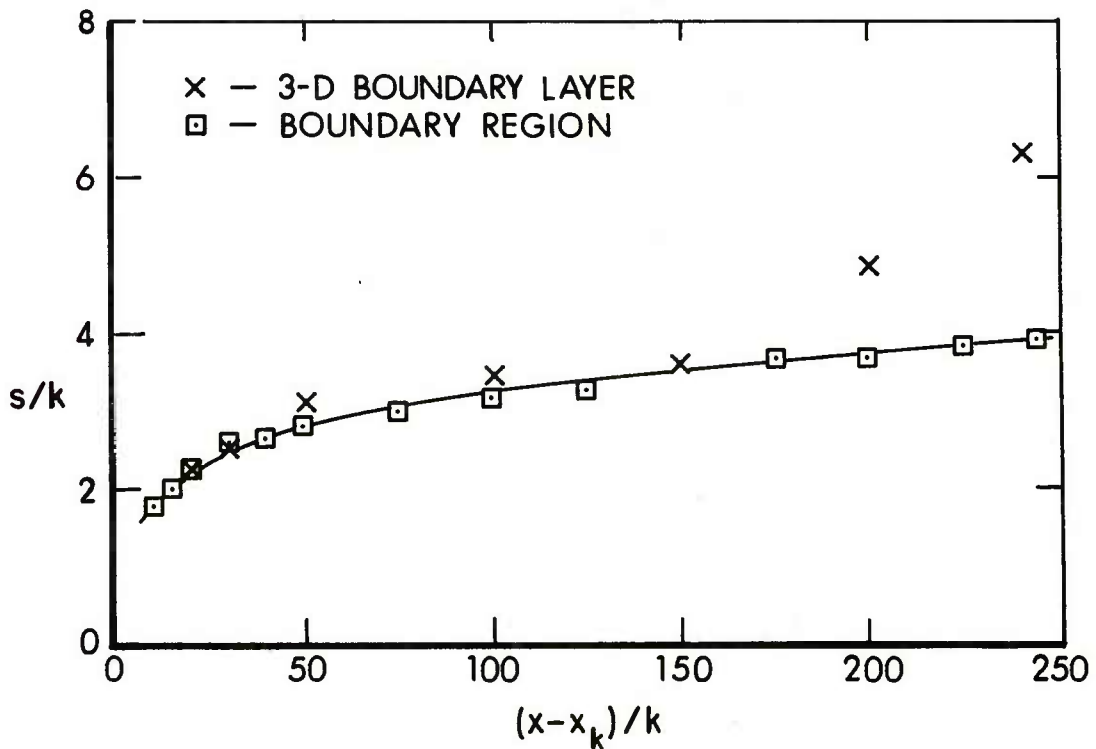


Figure 11. Comparison of Horseshoe Vortex Spacing: 3-D Boundary Layer (Scheme D) vs Boundary Region

LIST OF SYMBOLS

f_0, F_2	functions employed in formulation of initial plane data, Eq. (21)
k	height of cylindrical protuberance (=0.25 cm in expt.)
L	reference length for nondimensionalizing (= 1 cm)
p	pressure [g/(cm s ²)]
P	= $p/(\rho u_\infty^2)$
Re	= $\rho u_\infty L/\mu$ = Reynolds number (= 3467 in expt.)
Re_k	= $\rho u_\infty k/\mu$ = roughness Reynolds number (= 550 in expt.)
Re_{x_k}	= $\rho u_\infty x_k/\mu$ (= 2.08×10^5 in expt.)
s	2 times value of y at which $U = \frac{1}{2}(U_1 + U_2)$, Figure 2a [cm]
u, v, w	velocity components in the directions of $x, y,$ and $z,$ respectively [cm/s]
u_∞	free stream velocity (= 520 cm/s in expt.)
U, V, W	= $u/u_\infty, v/u_\infty, Re^{1/2} w/u_\infty,$ respectively
U_1, U_2	maximum and minimum values of $U,$ respectively, (Figure 2a)
U_B	Blasius flat plate boundary layer velocity, Eq. (20)
U_I, V_I	U and V at $X = X_I,$ plane of initial data
U_T	U -velocity function obtained by fitting Tani data, Eqs. (17) and (22)
x, y, z	rectangular coordinates: streamwise, spanwise, and normal to wall, respectively (Figure 1) [cm], origin at leading edge of flat plate
x_k	x -coordinate of cylindrical protuberance, Figure 1 (= 60 cm in expt.)
X, Y, Z	= $x/L, y/L, Re^{1/2} z/L,$ respectively
X_I	X -coordinate of initial data plane (= 62.5 in expt.)
β_T	function describing spanwise $V_I/U_I,$ obtained by fitting Tani data, Eqs. (18) and (22)
δ	boundary layer thickness, Figure 1 [cm]

LIST OF SYMBOLS
(Continued)

$\Delta X, \Delta Y, \Delta Z$	increments in X, Y, and Z in finite-difference equations, Appendix C
ϵ	= 0 for boundary layer, = 1 for boundary region, Eqs. (14), (15), and (23)
ζ_x	streamwise vorticity ($\partial W / \partial Y - \partial V / \partial Z$)
η	= $Z / (2 X_I)^{1/2}$, Eq. (19)
μ	viscosity of air [g/(cm s)]
ν	kinematic viscosity of air (= 0.15 cm ² /s in expt)
ρ	density of air [g/cm ³]

Subscript

i, j, k	indices identifying grid points, Eq. (25) and Appendix C
I	initial plane of data
k	front of cylindrical protuberance
T	Tani measurement
∞	free stream

Superscript

m	designator of iteration level
---	-------------------------------

APPENDIX A: TABLES OF f_0' , $\eta f_0''$, and F_2

η	f_0'	$\eta f_0''$	F_2
0.00	.0000	.0000	.0000
0.25	.1174	.1173	.2494
0.50	.2342	.2325	.4906
0.75	.3493	.3408	.7032
1.00	.4606	.4344	.8574
1.25	.5656	.5044	.9223
1.50	.6615	.5427	.8776
1.60	.6967	.5480	.8286
1.75	.7458	.5448	.7254
2.00	.8167	.5113	.4948
2.25	.8736	.4490	.2354
2.50	.9168	.3687	.0013
2.75	.9479	.2831	-.1671
3.00	.9691	.2031	-.2543
3.25	.9826	.1363	-.2691
3.50	.9907	.0855	-.2353
3.75	.9953	.0501	-.1795
4.00	.9978	.0275	-.1226
4.25	.9990	.0141	-.0759
4.50	.9996	.0068	-.0430
4.75	.9998	.0031	-.0224
5.00	.9999	.0013	-.0108
5.25	1.0000	.0005	-.0048

APPENDIX B: POLYNOMIAL COEFFICIENTS IN EQ. (22)

U_T	a_0	a_1	a_2	a_3
$0 < Y < 0.12$	4.150×10^{-1}	0.000×10^0	3.854×10^1	-2.141×10^2
$0.12 < Y < 0.3$	3.689×10^{-1}	4.444×10^0	-2.593×10^1	4.115×10^1
$0.3 < Y < 0.3015$	1.401×10^4	-1.397×10^5	4.645×10^5	-5.148×10^5
$0.3015 < Y < 2.5$	4.196×10^{-1}	2.336×10^{-1}	-1.042×10^{-1}	1.531×10^{-2}

$$2.5 < Y : U_T(Y) = U_T(Y = 2.5)$$

B_T (deg.)	b_0	b_1	b_2	b_3
$0 < Y < 0.05$	0.000×10^0	2.900×10^1	4.840×10^2	-1.032×10^4
$0.05 < Y < 0.2$	-2.759×10^{-1}	7.182×10^1	-8.978×10^2	2.394×10^3
$0.2 < Y < 0.375$	1.011×10^1	-1.543×10^2	5.846×10^2	-6.629×10^2
$0.375 < Y < 0.8$	-4.624×10^0	1.917×10^1	-2.624×10^1	1.189×10^1

$$0.8 < Y : B_T(Y) = 0.0$$

APPENDIX C: PCMI FINITE - DIFFERENCE EQUATIONS

Uncoupled linear finite-difference equations are constructed with the PCMI method by approximating U, V and W in Eqs. (14) and (15) as known constants, specified from either the extrapolated value or the value calculated at the previous iteration level. The coupling between equations and the nonlinearities of individual terms are approximated by the multiple-iteration process which updates U, V and W at each subsequent iteration level. The X-momentum difference equation is given by the tridiagonal system

$$a_{1j} U_{i+1,j,k-1}^{m+1} + b_{1j} U_{i+1,j,k}^{m+1} + c_{1j} U_{i+1,j,k+1}^{m+1} = d_{1j} \quad (C-1)$$

where

$$a_{1j} = -(W_{i+1,j,k}^m + W_{i,j,k}^m)/(8\Delta Z) - 1/(2\Delta Z^2) \quad (C-2)$$

$$b_{1j} = (U_{i+1,j,k}^m + U_{i,j,k}^m)/(2\Delta X) + 1/(\Delta Z^2) + \epsilon/(\text{Re } \Delta Y^2) \quad (C-3)$$

$$c_{1j} = -a_{1j} - 1/(\Delta Z^2) \quad (C-4)$$

$$\begin{aligned} d_{1j} = & U_{i,j,k} (U_{i+1,j,k}^m + U_{i,j,k}^m)/(2\Delta X) \\ & + (U_{i,j,k+1} - 2U_{i,j,k} + U_{i,j,k-1})/(2\Delta Z^2) \\ & - (W_{i+1,j,k}^m + W_{i,j,k}^m)(U_{i,j,k+1} - U_{i,j,k-1})/(8\Delta Z) \\ & - (V_{i+1,j,k}^m + V_{i,j,k}^m)(U_{i+1,j+1,k}^m - U_{i+1,j-1,k}^m + U_{i,j+1,k} \\ & - U_{i,j-1,k}^m)/(8\Delta Y) + \epsilon(U_{i+1,j+1,k}^m + U_{i+1,j-1,k}^m + U_{i,j+1,k} \\ & - 2U_{i,j,k} + U_{i,j-1,k}^m)/(2\text{Re } \Delta Y^2), \end{aligned} \quad (C-5)$$

with $\epsilon = 0$ in the 3D boundary layer approximation and $\epsilon = 1$ in the 3D boundary region approximation. The Y-momentum difference equation is given by the tridiagonal system

$$a_{2j} V_{i+1,j,k-1}^{m+1} + b_{2j} V_{i+1,j,k}^{m+1} + c_{2j} V_{i+1,j,k+1}^{m+1} = d_{2j} \quad (C-6)$$

where

$$a_{2j} = a_{1j}, \quad (C-7)$$

$$b_{2j} = b_{1j}, \quad (C-8)$$

$$c_{2j} = c_{1j}, \quad (C-9)$$

$$\begin{aligned} d_{2j} = & V_{i,j,k} (U_{i+1,j,k}^m + U_{i,j,k}) / (2\Delta X) \\ & + (V_{i,j,k+1} - 2V_{i,j,k} + V_{i,j,k-1}) / (2\Delta Z^2) \\ & - (W_{i+1,j,k}^m + W_{i,j,k}) (V_{i,j,k+1} - V_{i,j,k-1}) / (8\Delta Z) \\ & - (V_{i+1,j,k}^m + V_{i,j,k}) (V_{i+1,j+1,k}^m - V_{i+1,j-1,k}^{m+1} + V_{i,j+1,k} \\ & - V_{i,j-1,k}^{m+1}) / (8\Delta Y) + \epsilon (V_{i+1,j+1,k}^m + V_{i+1,j-1,k}^{m+1} + V_{i,j+1,k} \\ & - 2V_{i,j,k} + V_{i,j-1,k}^{m+1}) / (2\text{Re } \Delta Y^2). \end{aligned} \quad (C-10)$$

The continuity difference equation is given by

$$\begin{aligned}
 W_{i+1,j,k}^{m+1} = & W_{i+1,j,k-1} + (\Delta Z/4\Delta Y)(V_{i+1,j-1,k}^{m+1} \\
 & + V_{i+1,j-1,k-1}^{m+1} - V_{i+1,j+1,k}^{m+1} - V_{i+1,j+1,k-1}^{m+1}) \\
 & + (\Delta Z/2)[- a_3(U_{i+1,j,k}^{m+1} + U_{i+1,j,k-1}^{m+1}) + b_3(U_{i,j,k} + U_{i,j,k-1}) \\
 & - c_3(U_{i-1,j,k} + U_{i-1,j,k-1})]
 \end{aligned} \tag{C-11}$$

where

$$a_3 = 1/(X_{i+1} - X_i) + 1/(X_{i+1} - X_{i-1}), \tag{C-12}$$

$$b_3 = (X_{i+1} - X_{i-1})/[(X_i - X_{i-1})(X_{i+1} - X_i)], \tag{C-13}$$

$$c_3 = (X_{i+1} - X_i)/[(X_{i+1} - X_{i-1})(X_i - X_{i-1})], \tag{C-14}$$

In Eq. (C-11) the difference approximation for $\partial U/\partial X$ is based on a second-order accurate backward-difference formula for unevenly-spaced points involving three X-levels; the first step in X off the initial data plane requires a difference formula involving only two X-levels.

DISTRIBUTION LIST

<u>No. of Copies</u>	<u>Organization</u>	<u>No. of Copies</u>	<u>Organization</u>
12	Commander Defense Technical Info Center ATTN: DDC-DDA Cameron Station Alexandria, VA 22314	1	Director US Army ARRADCOM Benet Weapons Laboratory ATTN: DRDAR-LCB-TL Watervliet, NY 12189
1	Commander US Army Engineer Waterways Experiment Station ATTN: R.H. Malter Vicksburg, MS 39180	1	Commander US Army Aviation Research and Development Command ATTN: DRDAV-E 4300 Goodfellow Boulevard St. Louis, MO 63120
1	Commander US Army Materiel Development and Readiness Command ATTN: DRCDMD-ST 5001 Eisenhower Avenue Alexandria, VA 22333	1	Director US Army Air Mobility Research and Development Laboratory ATTN: SAVDL-D, W.J. McCroskey Ames Research Center Moffett Field, CA 94035
3	Commander US Army Armament Research and Development Command ATTN: DRDAR-TSS (2 cys) DRDAR-LC, Dr. J.Frasier Dover, NJ 07801	1	Commander US Army Communications Rsch and Development Command ATTN; DRDCO-PPA-SA Fort Monmouth, NJ 07703
6	Commander US Army Armament Research and Development Command ATTN: DRDAR-LCA-F Mr. D. Mertz Mr. E. Falkowski Mr. A. Loeb Mr. R. Kline Mr. S. Kahn Mr. S. Wasserman Dover, NJ 07801	1	Commander US Army Electronics Research and Development Command Technical Support Activity ATTN: DELSD-L Fort Monmouth, NJ 07703
1	Commander US Army Armament Materiel Readiness Command ATTN: DRSAR-LEP-L, Tech Lib Rock Island, IL 61299	3	Commander US Army Missile Command ATTN: DRSMI-R DRSMI-YDL DRSMI-RDK Mr. R. Deep Redstone Arsenal, AL 35809
1	Commander US Army Tank Automotive Research & Development Cmd ATTN: DRDTA-UL Warren, MI 48090	1	Commander US Army Tank Automotive Research & Development Cmd ATTN: DRDTA-UL Warren, MI 48090

DISTRIBUTION LIST

<u>No. of Copies</u>	<u>Organization</u>	<u>No. of Copies</u>	<u>Organization</u>
1	Commander US Army Jefferson Proving Ground ATTN: STEJP-TD-D Madison, IN 47250	1	Commander Naval Surface Weapons Center ATTN: DX-21, Lib Br Dahlgren, VA 22448
1	Commander US Army Research Office ATTN: Dr. R.E. Singleton P.O. Box 12211 Research Triangle Park, NC 27709	5	Commander Naval Surface Weapons Center Applied Aerodynamics Division ATTN: K.R. Enkenhus M. Ciment S.M. Hastings A.E. Winklemann W.C. Ragsdale Silver Spring, MD 20910
1	AGARD-NATO ATTN: R.H. Korkegi APO New York 09777	1	AFATL (DLDL, Dr. D.C. Daniel) Elgin AFB, FL 32542
1	Director US Army TRADOC Systems Analysis Activity ATTN: ATAA-SL, Tech Lib White Sands Missile Range, NM 88002	2	AFFDL (W.L. Hankey; J.S. Shang) Wright-Patterson AFB, OH 45433
3	Commander Naval Air Systems Command ATTN: AIR-604 Washington, DC 20360	4	Director National Aeronautics and Space Administration ATTN: D.R. Chapman J. Rakich W.C. Rose B. Wick Ames Research Center Moffett Field, CA 94035
2	Commander David W. Taylor Naval Ship Research and Development Cmd ATTN: H.J. Lugt, Code 1802 S. De los Santos Head, High Speed Aero Division Bethesda, MD 20084	4	Director National Aeronautics and Space Administration ATTN: E. Price J. South J.R. Sterrett Tech Library Langley Research Center Langley Station Hampton, VA 23365
		1	Director National Aeronautics and Space Administration Lewis Research Center ATTN: MS 60-3, Tech Lib 21000 Brookpark Road Cleveland, OH 44135

DISTRIBUTION LIST

<u>No. of Copies</u>	<u>Organization</u>	<u>No. of Copies</u>	<u>Organization</u>
2	Director National Aeronautics and Space Administration Marshall Space Flight Center ATTN: A.R. Felix, Chief S&E-AERO-AE Dr. W.W. Fowlis Huntsville, AL 35812	1	General Dynamics ATTN: Research Lib 2246 P.O. Box 748 Fort Worth, TX 76101
2	Director Jet Propulsion Laboratory ATTN: L.M. Mach Tech Library 4800 Oak Grove Drive Pasadena, CA 91103	1	General Electric Company, RESD ATTN: R.A. Larmour 3198 Chestnut Street Philadelphia, PA 19101
3	Arnold Research Org., Inc. ATTN: J.D. Whitfield R.K. Matthews J.C. Adams Arnold AFB, TN 37389	2	Grumman Aerospace Corporation ATTN: R.E. Melnik L.G. Kaufman Bethpage, NY 11714
3	Aerospace Corporation ATTN: H. Mirels R.L. Varwig Aerophysics Lab. P.O. Box 92957 Los Angeles, CA 90009	2	Lockheed-Georgia Company ATTN: B.H. Little, Jr. G.A. Pounds Dept 72074, Zone 403 86 South Cobb Drive Marietta, GA 30062
1	AVCO Systems Division ATTN: B. Reeves 201 Lowell Street Wilmington, MA 01887	1	Lockheed Missiles and Space Company ATTN: Tech Info Center 3251 Hanover Street Palo Alto, CA 94304
3	Boeing Commercial Airplane Company ATTN: G.M. Bowes M.S. 1W-82, Org B-8120 P.E. Rubbert, MS 3N-29 J.D. McLean, MS 3N-19 Seattle, WA 98124	3	Martin-Marietta Laboratories ATTN: S.H. Maslen S.C. Traugott H. Obremski 1450 S. Rolling Road Baltimore, MD 21227
3	Calspan Corporation ATTN: A. Ritter G. Homicz W. Rae P.O. Box 400 Buffalo, NY 14221	2	McDonnell Douglas Astronautics Corporation ATTN: J. Xerikos H. Tang 5301 Bolsa Avenue Huntington Beach, CA 92647

DISTRIBUTION LIST

<u>No. of Copies</u>	<u>Organization</u>	<u>No. of Copies</u>	<u>Organization</u>
2	McDonnell-Douglas Corporation Douglas Aircraft Company ATTN: T. Cebeci K. Stewartson 3855 Lakewood Boulevard Long Beach, CA 90801	2	Illinois Institute of Tech ATTN: M.V. Morkovin H.M. Nagib 3300 South Federal Chicago, IL 60616
2	Sandia Laboratories ATTN: F.G. Blottner Tech Lib Albuquerque, NM 87115	1	The Johns Hopkins University Department of Mechanics and Materials Science ATTN: S. Corrsin Baltimore, MD 21218
2	United Aircraft Corporation Research Laboratories ATTN: M.J. Werle Library 400 Main Street East Hartford, CT 06108	1	The Johns Hopkins University Applied Physics Laboratory ATTN: R.D. Whiting Johns Hopkins Road Laurel, MD 20810
1	Vought Systems Division LTV Aerospace Corporation ATTN: J.M. Cooksey Chief, Gas Dynamics Lab, 2-53700 P.O. Box 5907 Dallas, TX 75222	3	Massachusetts Institute of Technology ATTN: E. Covert H. Greenspan Tech Lib 77 Massachusetts Avenue Cambridge, MA 02139
1	Arizona State University Department of Mechanical and Energy Systems Engineering ATTN: G.P., Neitzel Tempe, AZ 85281	2	North Carolina State Univ Mechanical and Aerospace Engineering Department ATTN: F.F. DeJarnette J.C. Williams Raleigh, NC 27607
3	California Institute of Technology ATTN: Tech Library H.B. Keller, Mathematics Dept. D. Coles, Aeronautics Dept. Pasadena, CA 91109	1	Notre Dame University Department of Aero Engr ATTN: T.J. Mueller South Bend, IN 46556
1	Cornell University Graduate School of Aero Engr ATTN: Library Ithaca, NY 14850		

DISTRIBUTION LIST

<u>No. of Copies</u>	<u>Organization</u>	<u>No. of Copies</u>	<u>Organization</u>
2	Ohio State University Dept of Aeronautical and Astronautical Engineering ATTN: S.L. Petrie O.R. Burggraf Columbus, OH 43210	1	Southwest Research Institute Applied Mechanics Reviews 8500 Culebra Road San Antonio, TX 78228
2	Polytechnic Institute of New York ATTN: G. Moretti S.G. Rubin Route 110 Farmingdale, NY 11735	1	Texas A&M University College of Engineering ATTN: R.H. Page College Station, TX 77843
3	Princeton University James Forrestal Research Ctr Gas Dynamics Laboratory ATTN: S.M. Bogdonoff S.I. Cheng Tech Library Princeton, NJ 08540	1	University of California- Berkeley Department of Aerospace Engineering ATTN: M. Holt Berkeley, CA 94720
1	Purdue University Thermal Science & Prop Center ATTN: Tech Library W. Lafayette, IN 47907	1	University of California- Davis ATTN: H.A. Dwyer Davis, CA 95616
1	Rensselaer Polytechnic Institute Department of Math Sciences ATTN: R.C. DiPrima Troy, NY 12181	2	University of California- San Diego Department of Aerospace Engineering and Mechanical Engineering Sciences ATTN: P. Libby Tech Library La Jolla, CA 92037
1	San Diego State University Department of Aerospace Engr and Engr Mechanics College of Engineering ATTN: K.C. Wang San Diego, CA 92182	1	University of Cincinnati Department of Aerospace Engineering ATTN: R.T. Davis Cincinnati, OH 45221
1	Southern Methodist University Dept of Civil and Mechanical Engineering ATTN: R.L. Simpson Dallas, TX 75275	1	University of Colorado Department of Astro-Geophysics ATTN: E.R. Benton Boulder, CO 80302
		1	University of Hawaii Dept of Ocean Engineering ATTN: G. Venezian Honolulu, HI 96822

DISTRIBUTION LIST

<u>No. of Copies</u>	<u>Organization</u>	<u>No. of Copies</u>	<u>Organization</u>
2	University of Maryland ATTN: W. Melnik J.D. Anderson College Park, MD 20740	1	University of Wyoming ATTN: D.L. Boyer University Station Laramie, WY 82071
2	University of Michigan Department of Aeronautical Engineering ATTN: W.W. Wilmarth Tech Library East Engineering Building Ann Arbor, MI 48104	1	Virginia Polytechnic Institute and State University Department of Aerospace Engineering ATTN: Tech Library Blacksburg, VA 24061
1	University of Santa Clara Department of Physics ATTN: R. Greeley Santa Clara, CA 95053	1	Woods Hole Oceanographic Institute ATTN: J.A. Whitehead Woods Hole, MA 02543
3	University of Southern California Department of Aerospace Engineering ATTN: T. Maxworthy P. Weidman L.G. Redekopp Los Angeles, CA 90007	<u>Aberdeen Proving Ground</u>	
1	University of Texas Department of Aerospace Engineering ATTN: J.C. Westkaemper Austin, TX 78712	Dir, USAMSAF ATTN: DRXSY-D DRXSY-MP, H. Cohen	
1	University of Virginia Department of Aerospace Engineering & Engineering Physics ATTN: I.D. Jacobson Charlottesville, VA 22904	Cdr, USATECCM ATTN: DRSTE-TO-F	
1	University of Washington Department of Mechanical Engineering ATTN: Tech Library Seattle, WA 98195	Cdr/Dir, USA CSL ATTN: Munitions Div, Bldg. E3330 E.A. Jeffers W.C. Dee W.J. Pribyl	
		Dir, USACSL, Bldg. E3516, EA ATTN: DRCAR-CLB-PA	